Q21   # Toward understanding tectonic control on the M_w 8.8 2010 Maule Chile earthquake

Q12   M. Moreno [a,*], D. Melnick [b], M. Rosenau [a], J. Baez [c], J. Klotz [a], O. Oncken [a], A. Tassara [c], J. Chen [a,d], K. Bataille [c],
3   M. Bevis [e], A. Socquet [f], J. Bolte [g], C. Vigny [h], B. Brooks [i], I. Ryder [j], V. Grund [k], B. Smalley [l], D. Carrizo [m],
4   M. Bartsch [a], H. Hase [n]

5   [a] *Helmholtz-Zentrum Potsdam, Germany*
6   [b] *Universität Potsdam, Germany*
7   [c] *Universidad de Concepción, Chile*
8   [d] *Shanghai Astronomical Observatory, China*
9   [e] *Ohio State University, USA*
10   [f] *Université Joseph Fourier, Grenoble, France*
11   [g] *Technische Universität Berlin, Germany*
12   [h] *École Normale Supérieure, Paris, France*
13   [i] *University of Hawai'i, USA*
14   [j] *University of Liverpool, UK*
15   [k] *Sogeti High Tech GmbH, Hamburg, Germany*
16   [l] *University of Memphis, USA*
17   [m] *Universidad de Chile, Chile*
18   [n] *Geodetic Observatory TIGO, Concepción, Chile*

ARTICLE INFO

ABSTRACT

The Maule earthquake of 27th February 2010 ($M_w = 8.8$) affected ~500 km of the Nazca-South America plate boundary in south-central Chile producing spectacular crustal deformation. Here, we present a detailed estimate of static coseismic surface offsets as measured by survey and continuous GPS, both in the near- and far-field. Earthquake slip along the megathrust has been inferred from a joint inversion of our new data together with published GPS, InSAR, and land-level changes data using Green's functions generated by a spherical finite-element model with realistic subduction zone geometry. The combination of the data sets provided a good resolution, indicating that most of the slip was well resolved. Coseismic slip was concentrated north of the epicenter with up to 16 m of slip, whereas to the south it reached over 10 m within two minor patches. A comparison of coseismic slip with the slip deficit accumulated since the last great earthquake in 1835 suggests that the 2010 event closed a mature seismic gap. Slip deficit distribution shows an apparent local overshoot that highlight cycle-to-cycle variability, which has to be taken into account when anticipating future events from interseismic observations. Rupture propagation was obviously not affected by bathymetric features of the incoming plate. Instead, splay faults in the upper plate seem to have limited rupture propagation in the updip and along-strike directions. Additionally, we found that along-strike gradients in slip are spatially correlated with geometrical inflections of the megathrust. Our study suggests that persistent tectonic features may control strain accumulation and release along subduction megathrusts.

© 2012 Elsevier B.V. All rights reserved.

1. Introduction

Understanding the parameters controlling spatial patterns of pre- and coseismic crustal deformations is fundamental to test hypotheses on the recurrence and magnitude of great earthquakes. Coseismic slip is often heterogeneously concentrated within and around asperities that laterally segment a subduction zone. It remains unclear whether the asperity distribution is purely controlled by pre-stress conditions on the plate interface imposed by previous great earthquakes, or by tectonic features that influence the plate convergence induced strain in the overriding plate and its ability to store elastic energy. In any case, such mechanisms result in a modification of a simple elastic seismic-cycle model, where characteristic earthquakes occur periodically, towards a model with more variable recurrence patterns (e.g., Murray and Langbein, 2006; Murray and Segall, 2002).

The classical seismic gap concept, in which the recurrence history of past earthquakes suggests areas for potential ruptures, has been challenged after the occurrence of the great Tohoku-Oki earthquake (Heki, 2011). It has been shown that super cycle events (episodic multi-segment ruptures (e.g., Sawai et al., 2004)) can have a long   Q3

* Corresponding author.
    E-mail address: marcos@gfz-potsdam.de (M. Moreno).

recurrence interval (300–1500 yr) and release extremely high seismic moment ($>9\,M_w$), as was the case of the Valdivia 1960 earthquake (Cisternas et al., 2005). It follows that the seismic moment of the next great earthquake within such a super cycle might not be predictable from the slip deficit of the previous great earthquake. The latter point has been observed in the 2011 Tohoku-Oki (Avouac, 2011; Simons et al., 2011) and 2007 Sumatra (Konca et al., 2008) earthquakes; both events released less than the theoretically accumulated slip predicted from linear extrapolation of interseismic coupling.

Various geological features have been suggested to control stress buildup and release along megathrusts. These include mainly: (1) lateral variations in the frictional properties of the plate interface properties (e.g., Oleskevich et al., 1999; Prawirodirdjo et al., 1997);(2) bending and changes in the dip of the fault; inducing a differential stress regime (e.g., Nielsen and Knopoff, 1998) and possibly controlling the frictional behavior of the shallowest part of the megathrust (Wang and He, 2008); features of the subducting oceanic plate (e.g., Bangs et al., 2006); (3) the architecture and deformation behavior of the forearc (e.g., Rosenau and Oncken, 2009; Song and Simons, 2003); and (4) splay faults that may delimit the propagation of seismic rupture along the megathrust (e.g., Audin et al., 2008; McCaffrey and Goldfinger, 1995). The vast geodetic and geophysical data as well as the detailed structural information available for recent great earthquakes ($>8.5\,M_w$) (e.g., Simons et al., 2011; Subarya et al., 2006; Vigny et al., 2011) will enable us to test these hypotheses.

Here, we investigate the relation between slip patterns before and during the 2010 Maule earthquake ($M_w = 8.8$) with tectonic features of the Andean megathrust in South-Central Chile. First we derive an updated coseismic slip distribution based on complete GPS data set covering both the near- and far-field. Because megathrust geometry has a fundamental influence on slip distribution (e.g., Oglesby and Day, 2001), we use a spherical-earth finite-element model with realistic geometries adapted from geophysical data sets. Then we compare the spatial relationships of our slip distribution with the pattern of pre-seismic locking rate, upper and lower plate structures, and the geometry of the plate interface.

2. Previous slip models of the 2010 Maule earthquake

The great 2010 Maule earthquake ruptured ~500 km of the South-Central Chile subduction zone where the Nazca and South American plates converge at 66 mm/yr (Angermann et al., 1999) (Fig. 1). Rupture occurred on a mature seismic gap, the Concepción–Constitución gap, which was expected to fail on the basis of the slip deficit accumulated since major past earthquakes that occurred in 1835 (M~8.5) and in 1928 (M~8.0) in the south-central and north-central parts of the rupture respectively (Moreno et al., 2011; Ruegg et al., 2009). Published slip models (e.g., Lay et al., 2010; Lorito et al., 2011; Pollitz et al., 2011; Tong et al., 2010; Vigny et al., 2011), and coastal uplift data (Farías et al., 2010) suggest that the earthquake rupture zone extended from 34°S to 38.5°S, encompassing the two historical rupture zones and overlapping the southern part of the 1906 (M~=8.4) (Okal, 2005) and 1985 (M_w=7.8) (Barrientos, 1988) events, as well as the northern sector of the giant 1960 Valdivia earthquake (M_w=9.5) (Moreno et al., 2009) (Fig. 1).

By exploring the similarities between previous slip distributions and the pre-seismic locking derived from inversion of GPS observations of the previous decade, Moreno et al. (2010) suggested that pre-seismic, highly locked patches closely correlated with zones of high seismic slip. However, these coseismic slip models were principally based on teleseismic data and were not well constrained by geodetic observations in the near-field.

Clearly, a detailed slip model derived from a dense geodetic network is required for gaining insight into earthquake mechanisms and associated hazards. All previously published slip distributions for the Maule earthquake show a first-order pattern of two high-slip patches north and south of the epicenter. However, the slip magnitude and localization of these patches vary significantly between models, most probably as a consequence of using different observations (teleseismic, strong motion, InSAR, GPS, tsunami, far-field versus near-field) with varying sensitivity to details of the slip distributions. Moreover, spatial density, coverage and completeness of data sets vary considerably and neither a common fault geometry (planar versus curved) nor Earth model structure is shared among these models. Finally, the use of different inversion methods and hypocenter locations seemed to influence the slip distributions artificially. For instance, by comparing pre-seismic locking (Moreno et al., 2010) and coseismic slip derived from joint inversion of different observations, Lorito et al. (2011) suggested that the Maule earthquake did not fill the entire Constitución gap and consequently another major earthquake (M~8) in near future in that region might be imminent. Lorito et al.'s (2011) alarm was based on only three near-field GPS displacements inverted together with InSAR, tsunami and land-level changes data. Follow up studies using a denser set of near-field GPS displacements (Vigny et al., 2011), including this study, reached an opposite conclusion.

3. Main tectonic features of the Maule area

Four main structures segment the upper plate along the Maule segment: (1) A north–south trending Thrust Ridge (TR in Fig. 1) associated with splay faults has been imaged using multibeam bathymetry and reflection seismic data along the continental slope (Geersen et al., 2011). The Thrust Ridge coincides with the discontinuity between the frontal accretionary prism (consisting of unconsolidated sediments) and the continental framework made of paleo-accretionary structures (Contreras-Reyes et al., 2010; Moscoso et al., 2011). This structure is associated with a sharp geomorphic feature, suggesting young activity; (2) the Santa María Fault system (SMF in Fig. 1) consists of a series of back-thrusts extending between ~36°S to 37°S rooted in the plate interface (Melnick et al., 2006). At Santa María island (37°S), Melnick et al. (in press) documented coseismic surface fault ruptures associated with the SMFS. Presumably, this structure was also active during the late interseismic phase (Moreno et al., 2008); (3) the southern part of the Maule rupture zone overlaps with the area affected by the 1960 earthquake in the Arauco Peninsula; this is a region with a high Quaternary uplift rate, bounded to the south by a major crustal-scale splay fault system (Melnick et al., 2009), the Lanalhue Fault (LF in Fig. 1). Transpressional deformation along the Lanalhue Fault has been associated with collision of a forearc sliver, which also delimits the extent of the Valdivia seismotectonic segment; (4) At the northern boundary of the Maule rupture, eleven days after the mainshock, a shallow earthquake doublet (M_w=6.9 and M_w=6.7) (Comte et al., 2010) occurred on the Pichilemu Fault (PF in Fig. 1), which was a previously-unmapped fault (Ryder et al., in press). No surface rupture was associated with faulting, as evident from InSAR data.

The main oceanic features of the south-central Chile margin are the Valdivia and Mocha fracture zones. The former is a complex fracture zone system separating young oceanic crust (0–20 Ma) in the south, from old crust (>30 Ma) in the north, and intersects the margin at 39°S–41°S (Tebbens and Cande, 1997). The latter is currently subducting at the center of the Arauco Peninsula (38°S), north of the southern termination of the Maule rupture (Fig. 1).

4. Coseismic surface displacements from GPS

4.1. GPS data

A substantial GPS monitoring effort was underway prior to the Maule earthquake providing a dense coverage close to the south-central part of Maule rupture zone. We present new estimates of coseismic static offsets obtained from 47 survey (SGPS) and 8 continuous
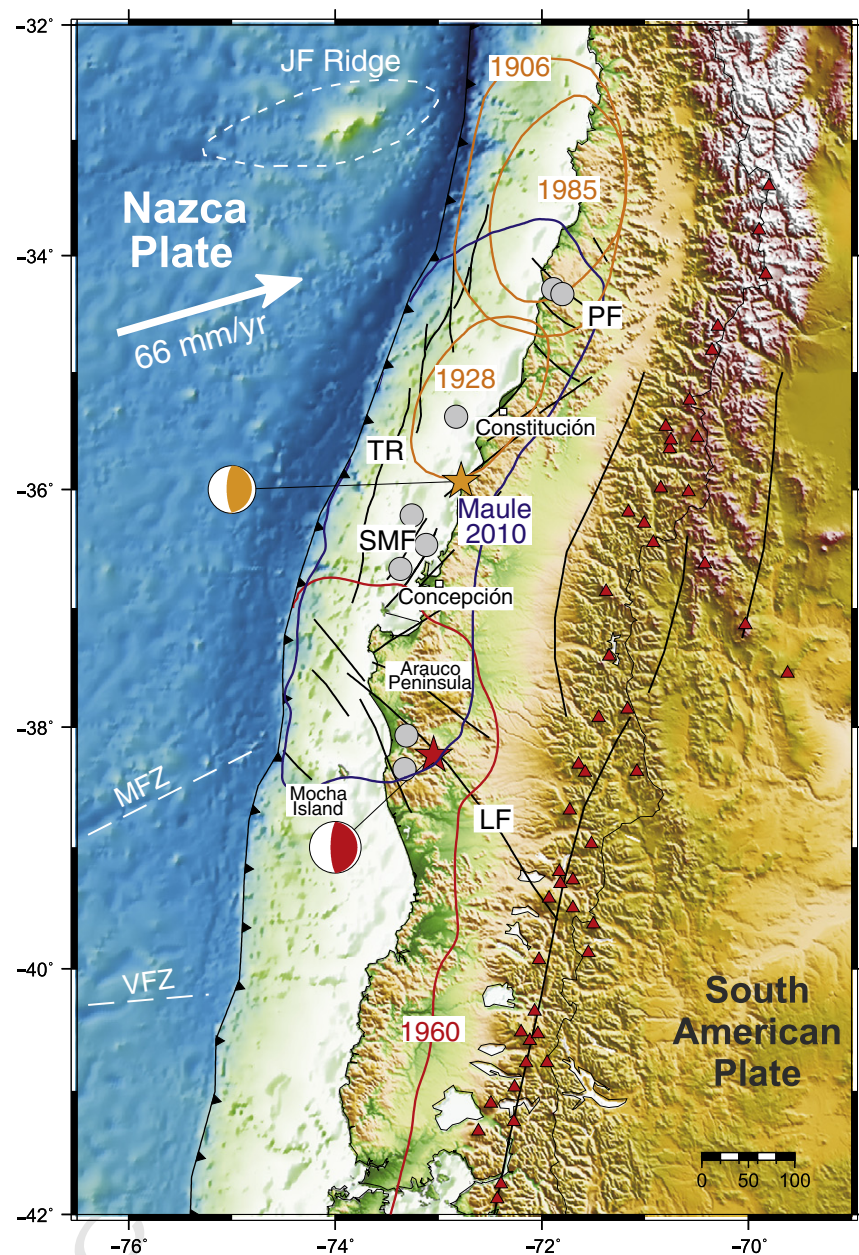
Fig. 1. Seismotectonic setting of the South-Central Chile megathrust. The rupture zone (>1 m) and fault plane solutions of the 2010 Maule and 1960 Valdivia (Moreno et al., 2009) megathrust earthquakes are shown in blue and red, respectively. Orange lines depict rupture zones of the 1906, 1928 and 1985 events. Gray circles are epicentral locations of largest aftershocks (M_w > 6.5). Black lines denote major upper plate faults consisting of the Thrust Ridge (TR), Santa María Fault (SMF), Lanalhue Fault (LF) and Pichilemu Fault (PF). Red triangles indicate active volcanoes. (For interpretation of the references to color in this figure legend, the reader is referred to the web version of this article.)

(CGPS) GPS around the Maule earthquake (Table S1, Fig. 1 and Fig. S1). The SGPS data were observed on existing benchmarks installed in the framework of the South American Geodynamic Activities (SAGA) project (Klotz et al., 2001) (45 sites) and Central Andes GPS Project (CAP) (Bevis et al., 2001) (2 sites). The CGPS stations were operated by the University of Concepción, Transportable Integrated Geodetic Observatory, University of Potsdam and GFZ-Potsdam. Far-field CGPS stations from the International GNSS Service (IGS) (32 stations) and Red Argentina de Monitoreo Satelital Continuo (RAMSAC) (43 stations) networks were also processed to achieve the best definition of a regional reference frame and to better constrain our coseismic slip model.

The SGPS data available prior to the 27th February 2010 Maule earthquake were collected mostly in December 2009 and re-observed within a few days to weeks after the event (Fig. S1, Table S1). We therefore applied corrections for interseismic and postseismic motions of these points to provide the best estimate of coseismic displacements. In the Maule region, The SAGA network has been observed in 8 regional campaigns over the last decade (Moreno et al., 2011), providing sufficient data to estimate the interseismic velocity directly at all SGPS points (Table S1). A dense array of CGPS network was installed in the region after the mainshock by Chilean, American, French, German and British groups (Bevis et al., 2010; Vigny et al., 2011). To correct the

postseismic motion of the SGPS sites, we processed 30 CGPS of this network spanning 150 days after the earthquake.

4.2. Data processing

We processed all data with Bernese GPS software V5.0 (Dach et al., 2007). The strategies were adapted from the system developed at the CODE (Center for Orbit Determination in Europe) and IGS Analysis Center for global network analysis. The main steps of the daily processing consisted of: (1) single point positioning based on pseudorange observations (receiver clock synchronization); (2) baseline definition using OBS-MAX strategy; (3) triple-difference solution applied for data cleaning, cycle slip detection and ambiguity setting; (4) ambiguity-float solution for post-fit residual screening and outlier rejection; (5) iterative ambiguity-float solution for the selection of fiducial stations (datum definition); (6) integer ambiguity resolution based on the Quasi-Ionosphere-Free (QIF) strategy; (7) ambiguity-fixed daily solution applying No-Net Translation (NNT) based on selected fiducial stations; and (8) definition of the reference frame.

Wherever possible the first-order effect of the ionosphere was eliminated using an ionosphere-free linear model. The second- and third-order effects were neglected in the processing. In pre-processing steps the troposphere effects were modeled with site-specific station parameters applying a tropospheric model and a mapping function. The troposphere parameters were pre-eliminated before saving daily normal equations. Thus, their connection at daily boundaries was not possible in the final combination. Whereas the effect on coordinate estimates in long-term combination is negligible, this approach significantly reduces requirements for the disk space and combination time.

The QIF ambiguity resolution strategy could be generally applied, which allows resolving L1 and L2 ambiguities even on long baselines. The ionospheric product from the CODE was introduced, and stochastic ionospheric parameters were estimated during the ambiguity fixing. The tropospheric parameters and a priori coordinates from daily ambiguity-float solution were introduced from the last iteration of the datum definition. The coordinates of one station were constrained for each cluster during the ambiguity resolution.

On average 80% ambiguities were fixed. After data cleaning and outlier rejection, the daily combination of ambiguity-float solution was used for fiducial station selection. Stations used as fiducials in the IGS05 reference frame (GLPS, BRAZ, CHPI, UNSA, CORD, SANT, CONZ, LPGS, RIOG, ISPA, ASC1,OHI2) were used to define an initial set, while the selection procedure was based on a minimum constrained solution, which was repeated until the set of fiducial stations provided sufficiently small residuals (6 mm).

The earthquake caused deformations at almost all the stations in the South America Plate. To achieve the best definition of regional reference frame, coordinates of the fiducial stations selected from previous step, were compared to their values under the IGS05 reference frame and the final selection of fiducial stations was done in an iterative way in order to eliminate outliers. The following criteria were used for the outlier detection: 8, 8 mm and 25 mm in North, East and Up. The RMS of residuals for the fiducial stations were 2.4 mm, 4.4 mm and 5.0 mm on average for North, East and Up, respectively.

4.3. GPS-derived coseismic displacements

The motions of SGPS sites were corrected for interseismic and postseismic deformations in both the horizontal and vertical components to minimize contamination of the coseismic displacement estimates. The interseismic strain field was well constrained by 2002–2009 GPS velocities in the area (Moreno et al., 2011), which were rather continuous and well fitted by linear trends. These velocities were used to extrapolate the position of the survey sites at the day of the earthquake (Table S1). Resulting interseismic corrections were in the order few centimeters (on average 2.64 cm for the longitudinal component).

The time-series of postseismic deformation analyzed here show rapid transient deformation immediately following the Maule earthquake (Fig. S2). The postseismic velocity decay during the first 150 days after the earthquake is well fitted (average $R^2 = 0.9$) by power law functions: $u(t) = a \times t^b + c$, where u is the position of the benchmark, t is time and a, b and c are the function coefficients (Fig. S2). Based on these functions, the displacement of each CGPS at the time of the SGPS observations could be estimated. Then, for the observation time of each SGPS, we interpolated a postseismic displacement field and estimated their postseismic motion. A standard error was assigned to each motion correction (Table S1). The SGPS data showed postseismic displacement corrections of no more than ~15 cm between the earthquake and the observation epochs (on average 4 cm for the longitudinal component), representing a small but significant fraction of static coseismic motions.

Our static coseismic displacements corroborate with motions obtained by Vigny et al. (2011) but provide additional valuable constraints on the coseismic displacement field, especially in the northern part of the rupture (where we fill a previous gap in GPS sites) and in the south-central part (where our GPS observations are concentrated) (Fig. 2 and Fig. S1). The maximum horizontal displacements occurred at 35°S and 37°S, with peaks of over 5 m north of Constitución and at Santa María island. Displacement vectors decreased in magnitude between these areas showing horizontal motions of only ~3 m around 36°S in the epicentral area. The hinge-line separating uplift from subsidence coincides with the coastline north of 37°S (Fig. 2), in agreement with the InSAR results (Tong et al., 2010) and field observations (Farías et al., 2010). Highest vertical variations were observed in the Arauco Peninsula, where coastal GPS sites recorded more than 1.80 m of uplift and inland sites subsidence of ~30–70 cm. The gross pattern of surface displacement shows convergence of near-field vectors towards the rupture area useful for deriving rupture limits at first-order. The earthquake deformation induced significant far-field deformation up to ~1000 km from the epicenter.

5. Coseismic slip model

5.1. Model setup

The plate interface geometry shows important variation both along-strike and dip in the area affected by the Maule earthquake (Contreras-Reyes et al., 2008, 2010; Haberland et al., 2009; Tassara et al., 2006). To avoid introducing slip artifacts due to geometry simplification and to reliably compare the slip patterns with the margin structure, we used a Finite Element model (FE-model) that takes into account the geometrical complexities of the Chile subduction zone. This is a spherical FE-model based on the same geometry and rheology used by Moreno et al. (2009, 2010), which permits a direct comparison of inter- and coseismic slip distributions.

Our FE-model extended to a depth of 500 km from 80°W to 60°W and 18°S to 45°S and consisted of elastic upper and subducting plates, and viscoelastic continental and oceanic mantles (Fig. 3). The thickness of the elastic oceanic plate was set to 30 km (Watt and Zhong, 2000), whereas the lower limit of the elastic upper plate was defined by the continental Moho. In the Maule area, the modeled continental crust was on average 40–45 km thick, with local extremes of 55 km (maximum), and 25 km (minimum) (Tassara et al., 2006). We specified a Young's modulus of 100, 120 and 160 GPa, for the continental, oceanic, and mantle layers, respectively. The Poisson's ratio was set to 0.265 and 0.30 for continental, and oceanic crust, respectively (Christensen, 1996).

Coseismic slip distributions of both dip-slip and strike-slip components were estimated using a damped linear least squares inversion based on FEM-generated Green's functions (Masterlark, 2003;
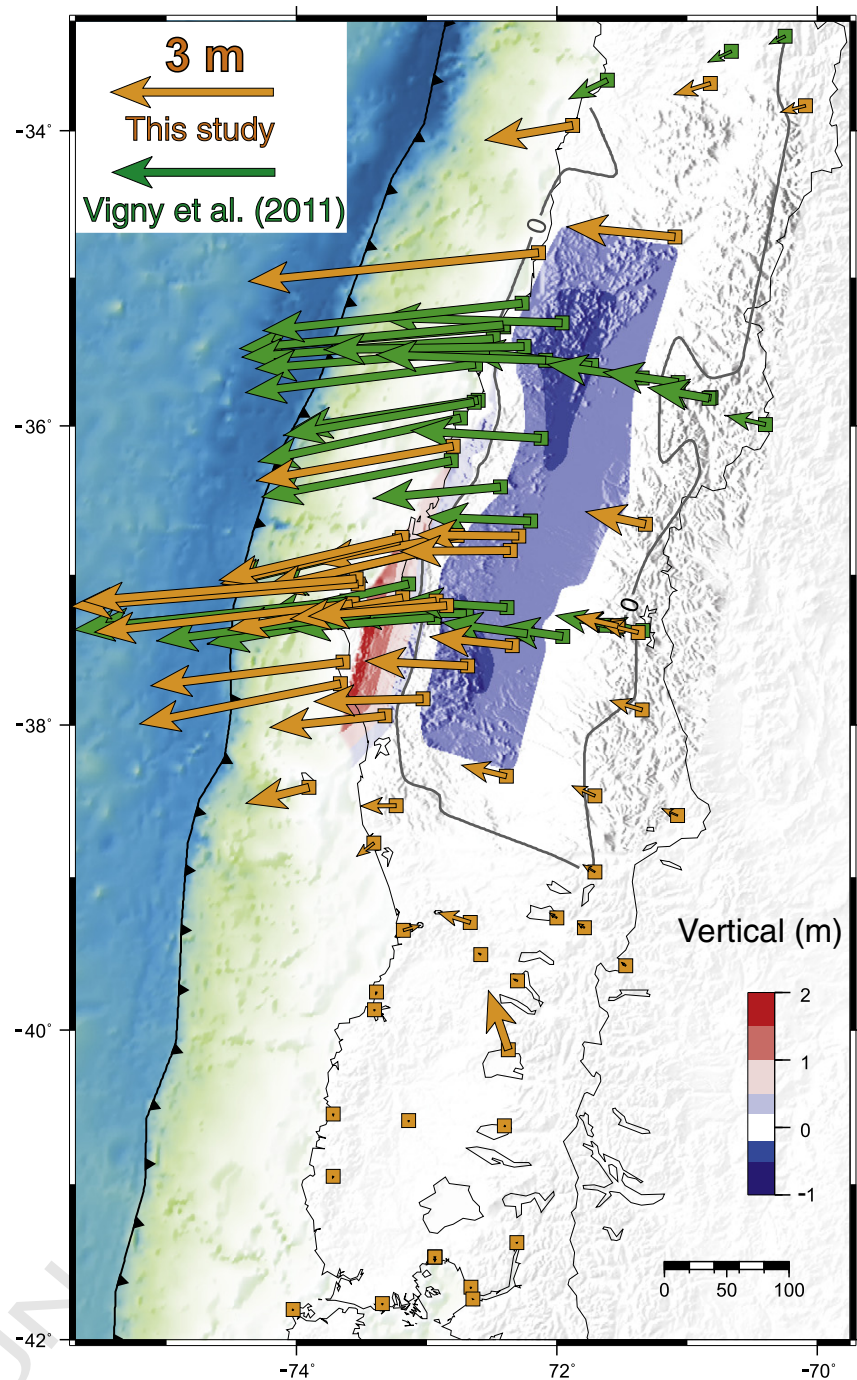
Fig. 2. Coseismic static displacements after the 2010 Maule earthquake. GPS displacements derived in this study are shown by orange arrows (Table S1). Published coseismic motions from Vigny et al. (2011) are depicted by green arrows. An interpolated grid shows the vertical component of the coseismic motion. Red and blue colors indicate uplift and subsidence, respectively. (For interpretation of the references to color in this figure legend, the reader is referred to the web version of this article.)

Masterlark and Hughes, 2008). Fault-slip was modeled using the split-node technique (Melosh and Raefsky, 1981) applying linear constraint equations. Nodes were restricted to the fault and consequently constrained to slide along the subduction plate interface. The upper surface of the model was assumed to be a stress-free surface, whereas lateral and basal boundaries were fixed from orthogonal displacements.

The slip distribution was constrained by a second order Laplacian operator to ensure that the slip differences between neighbor nodes in a curved and unsegmented fault are small, resulting in a stable solution (Moreno et al., 2009). We selected fault nodes localized above a depth of 70 km and between 32°S and 40°S. This resulted in the selection of 498 nodes. We jointly inverted our data with published GPS displacements (Vigny et al., 2011), InSAR data (Tong et al., 2010) and land-level changes (Melnick et al., 2012a). In doing so, the slip was inverted from 160 GPS displacements (3-components, i.e., 480 GPS observations), 820 and 1112 data points of line of sight (LOS) displacements from ascending and descending orbits, respectively,
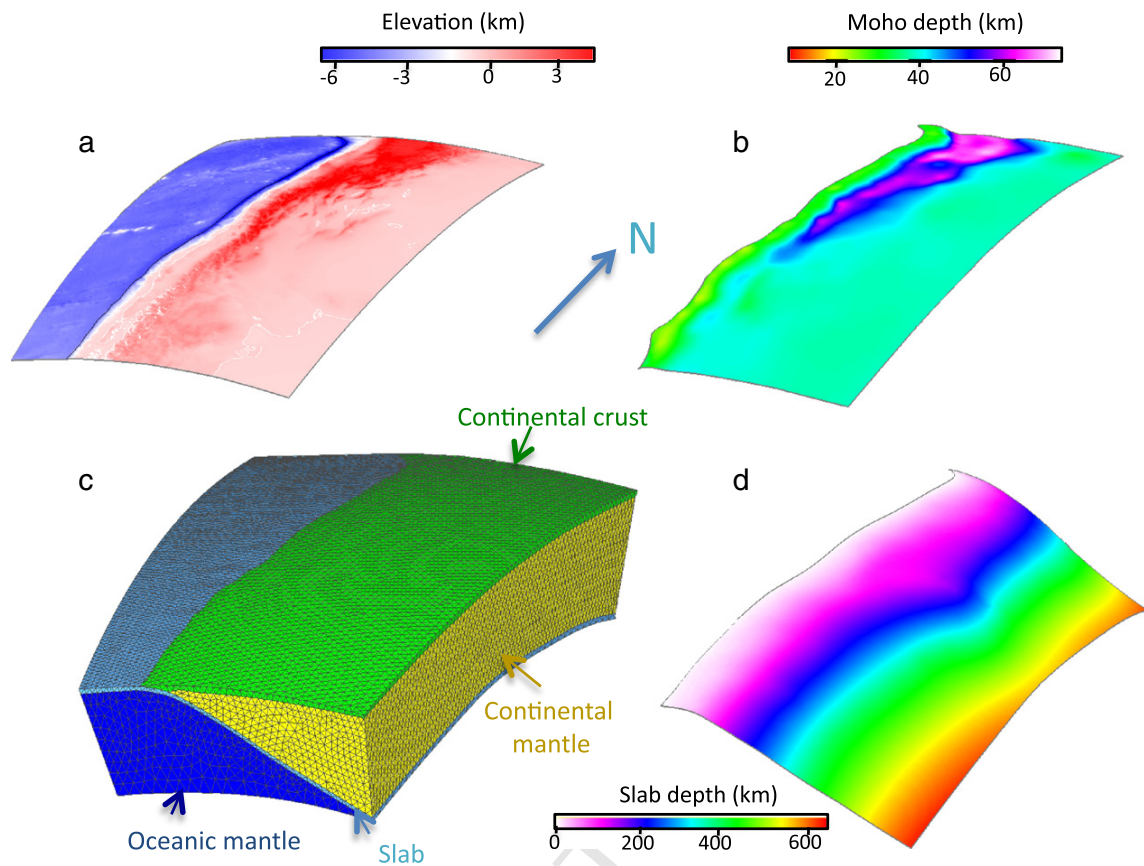
Fig. 3. 3-D model configuration. FE-models include topography and bathymetry, as well as a precise geometry of the slab and continental Moho, which were derived from combining available geophysical information. a) Topography and bathymetry introduced in the FE-model. b) Continental Moho discontinuity along the Chile subduction margin. c) Mesh structure of our FE-model. d) Upper surface of the plate interface used in this study.

and 34 vertical displacements from field observations. Inversions without constrains in the slip magnitude revealed that the slip amplitude was less than 20 m. To improve the model's resolution and to avoid unrealistic slip (e.g., Harris and Segall, 1987), we applied minimum and maximum slip constraints of 0 m and 20 m for the dip-slip component. We allowed right-lateral (negative values) and left-lateral (positive values) slip with a maximum amplitude of 5 m for the strike-slip component.

The preferred slip distributions were chosen from each individual data set using the trade-off curve between misfit and slip roughness for different smoothness values (e.g., Bürgmann et al., 2005). After we have chosen the optimal smoothing coefficient for each data set, we weighted the data sets in a joint inversion such that the smoothing parameters of individual data relate the system of equations (Kaverina et al., 2002; Price and Bürgmann, 2002). As a result, the joint inversion requires only one smoothing coefficient and determines data scale weights that maximize the fit to each data set. This approach is described by Kaverina et al. (2002).

5.2. Inversion results

Results for separate inversions of GPS, InSAR and land-level changes data, as well as the optimal joint inversion and their estimated errors (1-m gray contours) are shown in Fig. 4. The differences between solutions illustrate each data set's contribution to the optimal slip distribution. The solution based on the InSAR data (ascending and descending LOS) underestimates the slip south of 36°S, where near-field GPS offsets demand higher slip. The maximum slip was located in the northern part of the rupture and was 16.6 m for the InSAR case; 15.7 m from GPS. The minor difference may indicate a small postseismic contamination on the InSAR data, which has not been corrected and is related to the $M_w = 6.9$ and $M_w = 6.7$ aftershocks that occurred on 11th of March 2010 in the Pichilemu Fault (Comte et al., 2010; Ryder et al., in press). Important constraints in the southern part of the rupture have been provided by land-level measurements based on an intertidal organism (Melnick et al., 2012a). Assuming that measured coastal uplift is purely a result of elastic rebound and not complicated by local faulting in the upper plate, the solution based on land-level changes requires higher slip in the south (up to 12 m) along a larger area than for inversions based only on space geodetic observations (Fig. 4).

To explore the ability of our model to resolve the slip on the fault nodes, we computed the resolution matrix (Menke, 1989) for each individual data set (Fig. S3). When the diagonal of the resolution matrix equals the identity matrix, the estimated model is perfectly resolved. The resolution of slip distribution inferred using only GPS data is low (<0.50) along the shallow part of the fault and improves in the down-dip direction. Better resolution is achieved in the southern part of the rupture where the GPS network is denser, and extends farther updip. In the case of the InSAR inversion, the fault slip is relatively well resolved (>0.75), providing a resolution over 0.5 in the updip part of the model. The spatial resolution of the land-level changes inversion is very low; only the fault slip in the Arauco Peninsula is resolved. The spatial resolution improves with the joint inversion, which gives a better-resolved distribution of slip in the offshore part of the model (>0.50).
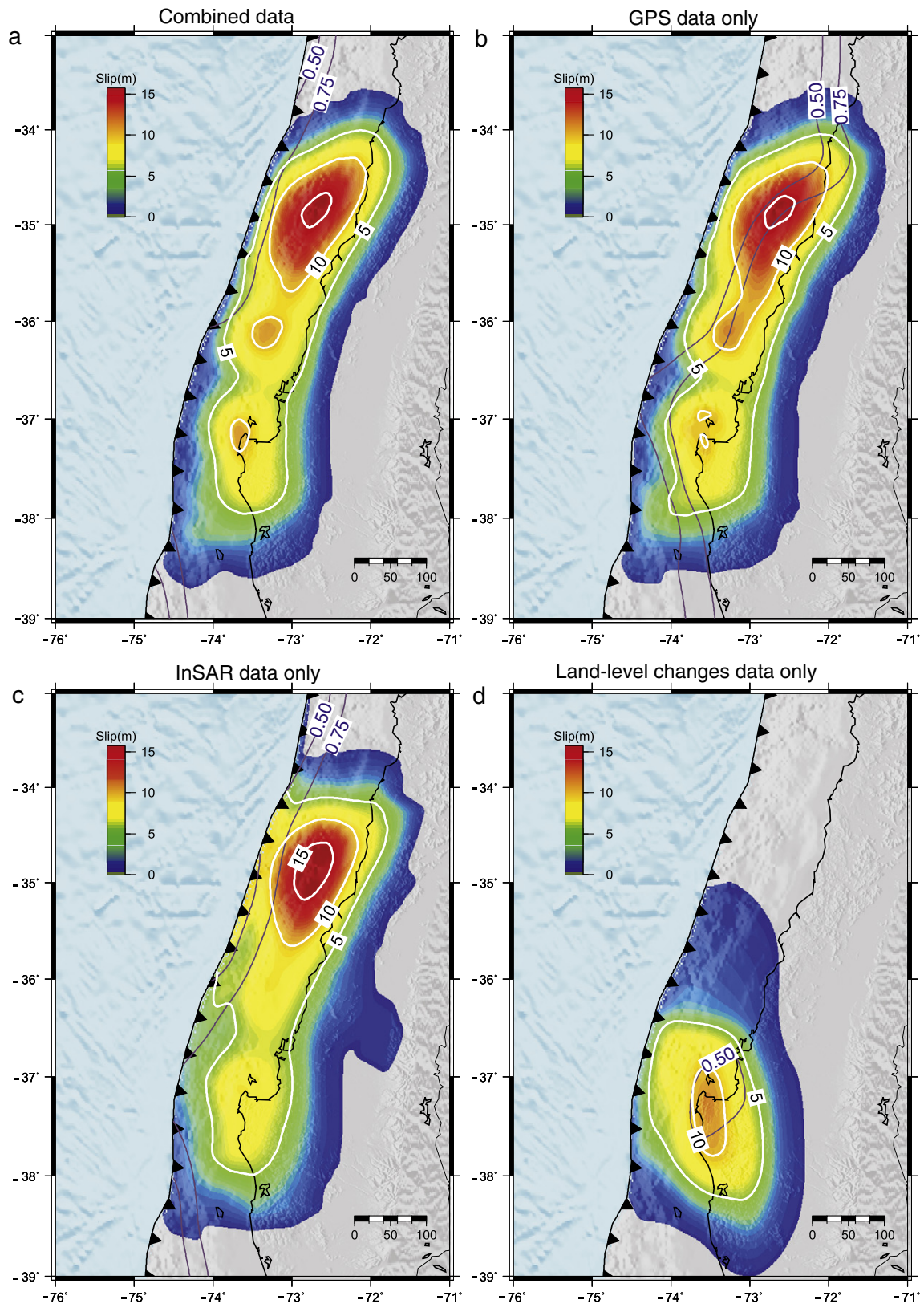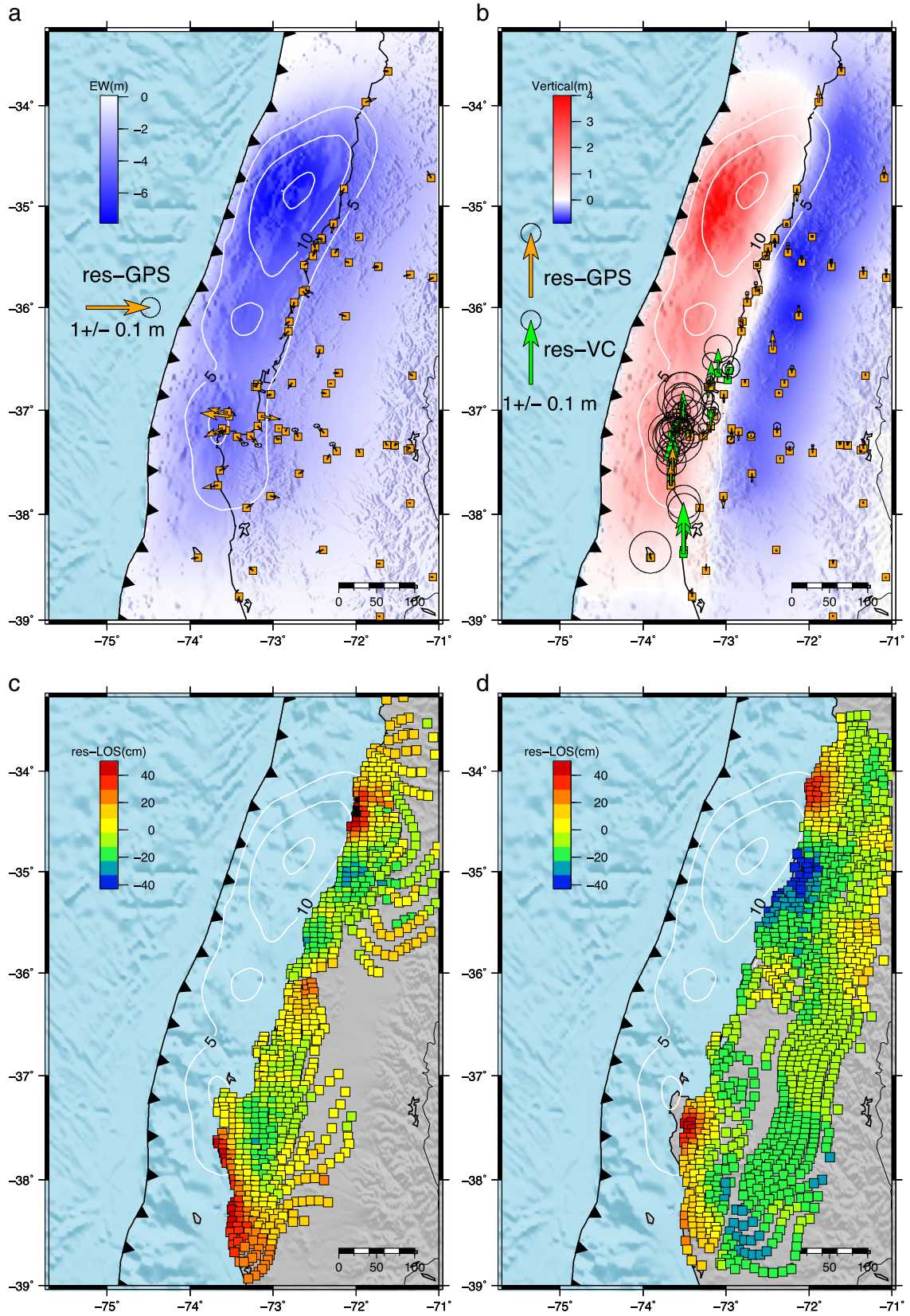
Fig. 4. Total coseismic slip obtained by using different data set. a) Joint inversion of GPS, InSAR and land-level changes. b) Slip model from inversion of GPS data alone. c) Slip model from inversion of InSAR data alone. d) Slip model from inversion of land-level changes alone. Gray contours show the resolution for each inversion.
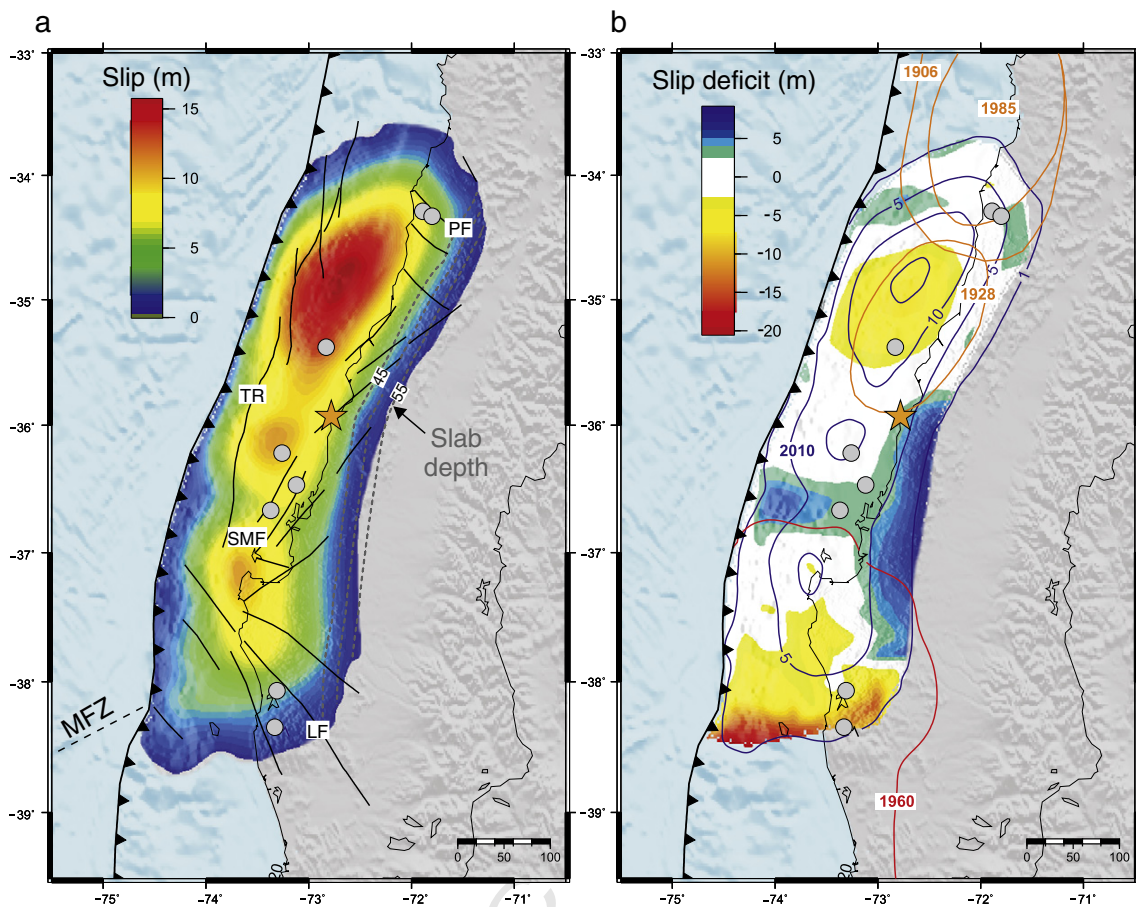
Fig. 6. a) Preferred coseismic slip model for the 2010 Maule earthquake. Black lines denote the Thrust Ridge (TR), Santa María Fault (SMF), Lanalhue Fault (LF) and Pichilemu Fault (PF). Gray circles are epicentral locations of largest aftershocks (M_w > 6.5). Dashed gray lines at the down-dip of the rupture depict the slab depth (5-m contours). b) Slip deficit estimation along the rupture area of the Maule earthquake. Shown are the rupture zones of the 1906, 1928, 1985, 1960 and 2010 earthquakes.

Results indicate that the GPS, InSAR and even the land-level observations alone give reasonable first-order representations of the main characteristics of the fault slip distribution. The weight scale for the joint inversion was estimated by determining the optimal model that does not significantly vary the fit of the individual data sets. The relative weights that stabilize the fits were chosen to be 0.5, 0.25 and 0.25 for the GPS, InSAR and land-level data. With these values, the fit to the GPS, InSAR and land-level data are reduced by less than 2%, 5%, and 4%, respectively. The combined solution fits the GPS, InSAR and land-level observations very well in terms of both direction and amplitude (Fig. 5). It produced a RMS of 0.15 m, 0.1 m, 0.14 m, and 0.35 m for the horizontal GPS, vertical GPS, LOS, and land-level data, respectively.

By using an average shear modulus of 40 GPa, the seismic moment of the optimal slip model is 2×10^{22} N m (M_w = 8.8) consistent with the seismological estimate (http://neic.usgs.gov). Our results also confirm that the rupture was mostly released in the down-dip direction, with a small component of strike-slip (Tong et al., 2010) (Table S2). Accordingly, the rupture has a multimodal pattern with a mean slip of 5.8 m. The optimal slip model exhibits a concentration of high slip in the north-central part of the rupture with slip up to 16 m, similar to previously published studies (Figs. 4, 6a, Table S2).

Two secondary asperities with slip over 12 m were found at 36.1°S and 37°S. The rupture bridged the areas between the primary and secondary asperities with rather low slip (<5 m) immediately north of the epicenter and at the latitude of Concepción city (36.85°S).

The down-dip extension of the rupture region (defined by the 1-m slip contour) reached depths of 55 km and 50 km in the north-central and south-central parts of the rupture zone, respectively (Fig. 6a). The 5-m slip contour nearly coincides with the coastline north of 37°S. In the Arauco Peninsula, slip larger than 5 m propagated up to 50 km inland of the coastline. At the northern patch, large slip concentrated beneath the continental shelf and triggered as much as 5 m of slip at shallow depth near the trench. Apparently, little or no slip is predicted near the trench axis by our model in the southern part of the rupture zone (no slip is required by the data).

The slip model produces a maximum of 7.90 m of trenchward motion, 4.02 m of uplift, and 0.85 m of subsidence (Fig. 5a–b). Major horizontal GPS residuals were found at Santa María island, where the model predicted less trenchward displacement than those recorded by GPS stations. However, a greater amount of slip in this area produces extra displacements in the coastal sites. In a similar way, land-level changes demand higher slip beneath Arauco Peninsula than the model prediction, but a higher level of slip

Fig. 5. Residuals between the observed and predicted displacements obtained from the optimal joint inversion. a) Residuals from horizontal GPS observations (orange arrows). A grid shows the east–west ground motion predicted by the model. b) Residuals from vertical GPS observations (orange arrows) and from land-level changes data (green arrows). A grid shows the vertical ground motion predicted by the model. c–d) Residuals from LOS observations. (For interpretation of the references to color in this figure legend, the reader is referred to the web version of this article.)

induces a misfit with the horizontal GPS displacements. It is note-worthy that the residuals from LOS data show the effect of after-shock deformation in the Pichilemu region as well as in an area that requires higher LOS displacements (principally vertical compo-nent of motion) along the southern coast of the Arauco Peninsula (Fig. 5c–d).

6. Discussion

6.1. Closure of the Concepción–Constitución seismic gap

Based on a compilation of historical accounts, the Maule earth-quake has been described as being similar to its predecessor in 1835 (M~8, (Lomnitz, 2004)), in terms of land-level changes, tsunami in-undation, and intensity distribution (Cisternas et al., 2010). Large earthquakes within or partially overlapping with the Maule rupture zone occurred in 1906, 1928, 1960 and 1985 (Fig. 1). These events released only a small fraction of the slip deficit accumulated after 1835 in the region. Assuming that the locking distribution observed during the decade preceding the event is representative for the whole inter-seismic time period (i.e. that the locking pattern is time indepen-dent), the slip deficit theoretically accumulated since 1835 can be calculated as the product of time, plate convergence (66 mm/yr) and degree of locking. The cumulative coseismic slip of the 1906, 1928, 1960, 1985 and 2010 events has to be subtracted from the previous product to obtain a meaningful slip deficit value (Fig. 6b). Because of the uncertainties of the historical slip distributions, as well as uncertainties in our inversions of pre-seismic locking and coseismic slip (Fig. 4), slip deficits below 2.5 m are considered in-significant. Today slip deficit distribution throughout the 2010 rup-ture zone suggests that this earthquake released most of the strain accumulated since 1835, i.e. that the Maule earthquake closed the Concepción–Constitución seismic gap at first-order.

6.2. Spatial relation between coseismic slip and interseismic locking rate

Here, we use our geodetically derived slip model, which is method-ologically compatible with the interseismic locking model of Moreno et al. (2010) to re-evaluate the spatial relationship between locked patches and asperities (Figs. 7, 9 and Fig. S4). Principally, the locking distribution showed two main high locked patches (>0.75) in the north and south of the epicenter, which were separated by an area of reduced locking rate (<0.75). According to our analysis, the earthquake rupture affected areas that had 0.70 locking rate on average. Patches that experienced high slip (>10 m) exclusively concentrated in areas with a mean of 0.80 locking rate (Fig. S4). The northern asperity over-laps with the area of reduced preseismic locking and correlates with a high gradient of locking. The southern two asperities spatially coincide with patches of high locking. The southern end of the rupture zone overlaps an area where the degree of locking was low (Fig. 7), which may have arrested further southward propagation of the rupture.

The locking patches over the decade preceding the Maule earth-quake are not the blueprint copy of high-slip regions, but are roughly coincident. Similar first-order spatial correlation but second-order incongruencies of interseismic locking and coseismic rupture extent has been found for the 2011 Tohoku-Oki earthquake (Loveless and Meade, 2011; Ozawa et al., 2011). Consequently, this correlation indi-cates a first-order persistency of asperities during the seismic cycle, which thus can be use to anticipate the maximum possible size of an earthquake in a particular region.

In contrast to the teleseismic inversions used by Moreno et al. (2010) to calculate a slip deficit close to zero throughout the 2010 Maule rupture area, coseismic slip inversions based at least partially on data accumulating deformation over longer time increments (minutes to days like the geodetic observations used here) seem to indicate an apparent overshoot (with respect to the theoretical
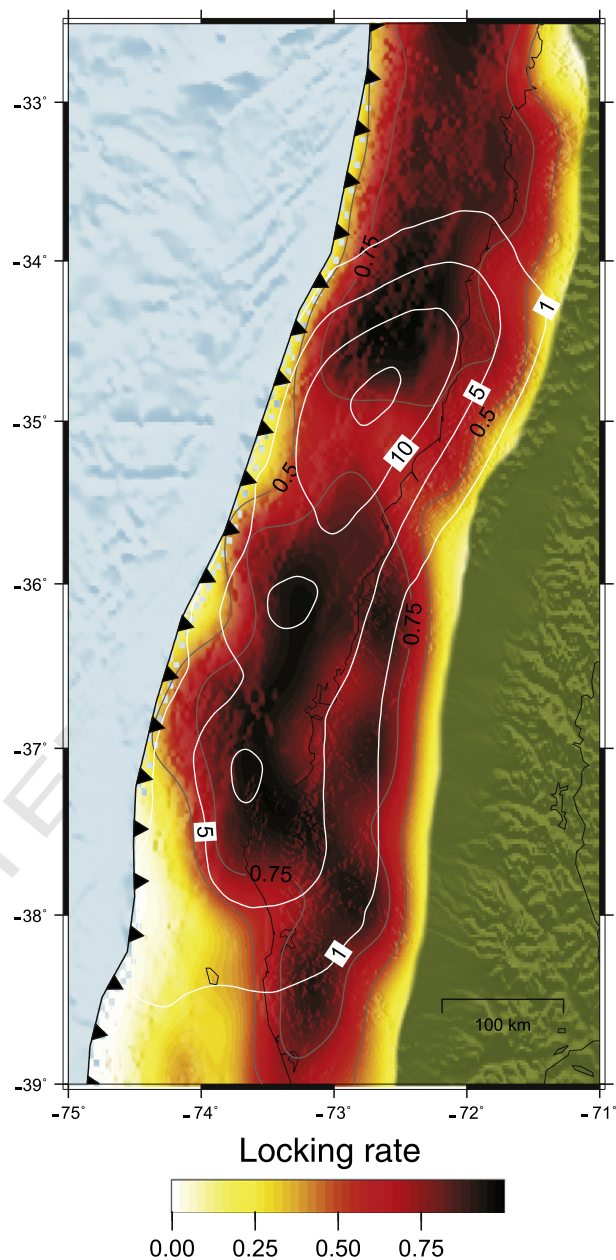

Fig. 7. Coseismic slip distribution, shown with 5-m slip contours, overlain on the lock-ing rate distribution, which is also shown by brown 0.25-rate contours (Moreno et al., 2010).

slip deficit since 1835) in the region which was not fully locked in the decade before the 2010 event. We speculate that part of this incongruence might be due to rather slow slip and rupture propaga-tion in the creeping section not detected by teleseismic observa-tions. This is corroborated by spatial variations of the frequency content radiated from the earthquake area (Wang and Mori, 2011).

An important and puzzling implication of the slip budget estimate is that the northern region and the Arauco Peninsula released more slip that may have been accumulated since 1835. Even if we assume that during the entire interseismic period the plate interface was fully locked, a negative slip deficit characterizes the areas affected by the 1928 and 1960 events. The negative slip deficit might indicate a slip deficit inherited from a pre-1835 interseismic period, as suggested for

the 1960 earthquake by Cisternas et al. (2005) or, an apparent local overshoot. The latter should result in strong normal faulting activity in the near-field or even along the plate interface as observed during the 2011 Japan earthquake (Yagi and Fukahata, 2011). While the largest aftershock was indeed a normal faulting event in the crustal forearc wedge (Ryder et al., in press), normal faulting along the plate interface has not been reported yet to our knowledge.

More significant slip deficit larger than 5 m has been found along the down-dip portions of the rupture zone between 36°S and 38°S (Fig. 6b), where interseismic GPS vectors demanded a deeper and wider locked zone (Moreno et al., 2010). If the deep locking was real, the slip deficit is likely to be released by deep afterslip in the aftermath of the 2010 earthquake. This interpretation is qualitatively consistent with the distribution of afterslip inferred from GPS observations by Vigny et al. (2011). However, their reported afterslip during the first two weeks amounted to only a few decimeters and it seems unlikely that prolonged afterslip will counter balance the > 5 m of slip deficit suggested by our analysis. Extrapolating the slip rate of the first two weeks (0.25 m/week) based on a general power law decay function suggests that only about one tenth of the apparent deep slip deficit is likely to be balanced by afterslip. However, we cannot discard that creep transients, silent slip, or deep earthquakes might contribute to future megathrust slip balancing the seismic cycle slip budget. Alternatively, the slip deficit at the down-dip of the rupture might be artificial and a result of inaccuracies in the interseismic model, which is purely elastic, disregarding the viscoelastic behavior of the mantle. The latter may influence the down-dip limit, and thus width of the locked zone as shown by Wang et al. (2003).

A small region of significant slip deficit (> 5 m) exists at shallow depth forming a narrow fringe north of 37°S close to the trench. Two major aftershocks ($M_w = 6.7$ and $M_w = 6.9$) have occurred in this region (Fig. 6a); events that may have released part of this slip deficit. The same region was affected by an important afterslip immediately after the Maule earthquake (Vigny et al., 2011), indicating that the slip deficit may also have been released aseismically.

6.3. Search for a tectonic control

The above discussion points to a first-order similarity and persistence of patterns of slip and locking rate. The persistence of such a correlation over more than one seismic cycle would, however, require a mechanism that localizes stress buildup over longer time scales. To explore the possible tectonic control on the Maule earthquake rupture, we compared the slip patterns with upper and lower plate structures as well as with the geometry of the plate interface.

During a great interplate faulting event, splay faults can play a key role in controlling fluid pressurization (Boutareaud et al., 2008). Hence, the hydraulic behavior of splay faults may induce variations of shear strength and may promote dynamic slip weakening along the splay fault. Our proposed dislocation model reveals north of 37°S a concentration of shallower high slip (> 10 m) that abruptly decays seaward, coincidentally at the position of the Thrust Ridge associated with a splay fault system that straddles the edge of the continental slope (Figs. 1 and 6a) (Geersen et al., 2011). A sharp lateral gradient in the number of aftershocks has been observed across this splay fault (Lange et al., in press), suggesting a boundary between seismic and aseismic behaviors. Similarly, Moscoso et al. (2011) image a frontal accretionary prism ~40–50 km wide offshore Maule region, which is spatially coincident with the updip-aseismic region of plate interface. Vigny et al. (2011) proposed that slip reached the trench in this region; however, neither their nor our slip models have the resolution necessary to resolve near-trench slip. The rupture could have stepped up along the thrust-ridge or propagated to the trench. Based on the lack of aftershocks up-dip of the thrust ridge, we favor the step up process.

The Santa María Fault (Fig. 6a) is also spatially related with an area of reduced coseismic slip in the plate interface. Apparently, both splay faults may have influenced the distribution of coseismic slip for the Maule earthquake, by converting part of the elastic interseismic strain accumulated in the upper plate into plastic permanent deformation (Melnick et al., in press).

Though the slip distribution of the Maule earthquake does not show a particular spatial relation with the Lanalhue Fault, the high magnitude of uplift south of Arauco Peninsula from land-level changes (Melnick et al., 2012), a feature that the slip model cannot reproduce, may be tentatively associated with coseismic motion along this blind fault. A region of large misfit between model prediction and vertical observations is also shown by the residuals of LOS aligned with the Lanalhue Fault, which demand higher deformation or another mechanism than only slip along the interplate zone (Fig. 5c–d). However, fits to GPS data are practically insensible to possible slip along this crustal fault, which would involve gradients of vertical motions.

Features of the oceanic plate may potentially influence slip patterns. However, the slip distribution is not correlated with any first-
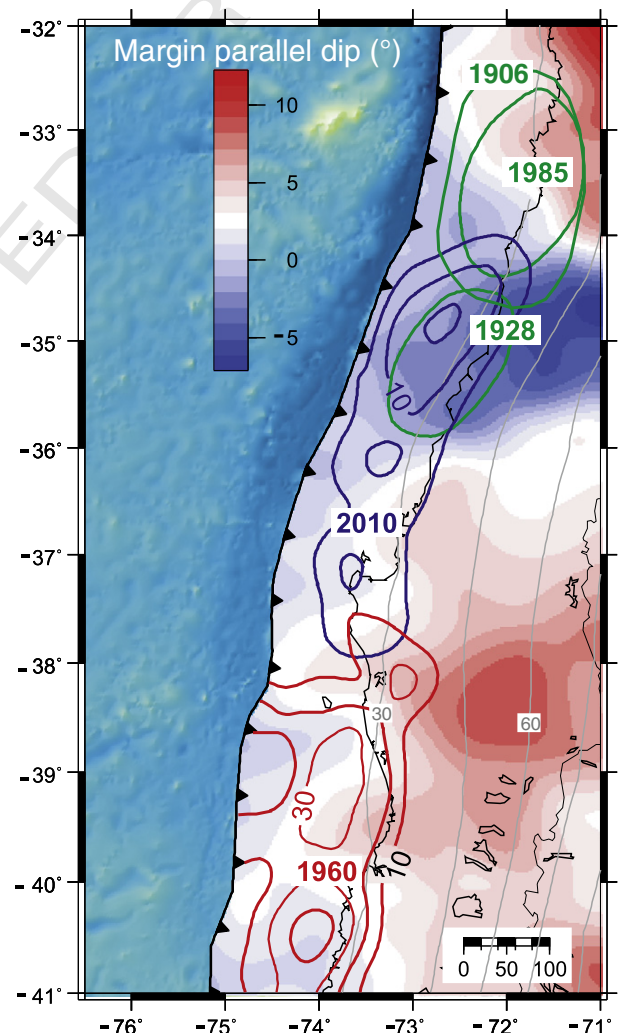

Fig. 8. Slab dip calculated in a direction parallel to the margin. Shown are the rupture zones of the 1906, 1928, 1985 (green lines), 1960 (10-m red contours) and 2010 (5-m blue contours) earthquakes. Gray 30-m contours indicate the slab depth. Directional slab dips were calculated using the grd gradient function of the GMT software (http://gmt.soes.hawaii.edu). (For interpretation of the references to color in this figure legend, the reader is referred to the web version of this article.)
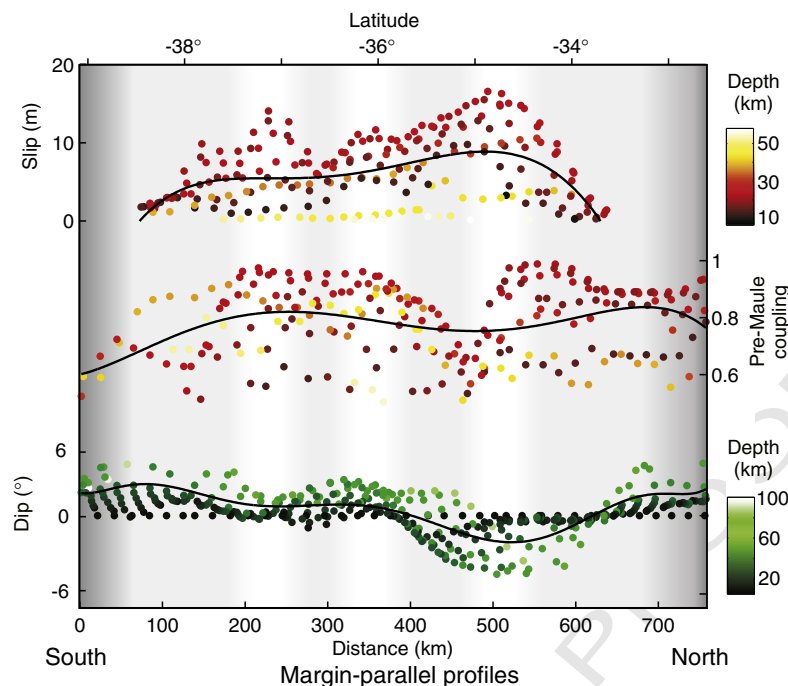
Fig. 9. Margin-parallel profiles of coseismic slip, interseismic locking rate and margin-parallel dip of the slab. Points are colored by their depth. (For interpretation of the references to color in this figure legend, the reader is referred to the web version of this article.)

order oceanic feature. The rupture stopped ~100 km to the south of the Juan Fernandez Ridge and propagated across the Mocha fracture zone. Our findings disagree with the recent work of Sparkes et al. (2010) that suggested control of bathymetric features on rupture extent along the Chilean margin.

Along-strike inflections and curvature of the slab can have an important effect on the dynamics of the earthquake processes (rupture propagation, e.g., Harris et al., 1991) and can cause the normal stress on the fault to vary with time due to the fact that the slab moves along a curved interface (e.g., Nielsen and Knopoff, 1998). In an attempt to explore the possible influence of the geometry of the plate interface on the pattern of inter- and coseismic strain, we calculated the directional gradients of the slab dip. One clear correlation is found between the slip distribution and slab dip gradients parallel to its strike (Figs. 8 and 9). Dip gradients in the down-dip sense do not show correlation with the interseismic and coseismic slip patches. High coseismic slip was mostly released in areas with negative margin parallel dip (Fig. S4). Highly locked patches are principally observed in areas where the slab plane has not major inflections. In turn, low locking patches coincide with lateral gradients of slab dip.

The northern slip maxima is well confined by an area where the slab plane shows a major along-strike inflection (34°S–36°S), which is reflected mostly in the down-dip of the rupture. In this region, the concave up portion of the plate boundary correlates with a local minimum in pre-Maule coupling (Fig. 9 and Fig. S4). Negative slip deficit, which represents areas that released more slip than the theoretically slip estimated from the locking model, coincides with major lateral gradients of slab dip. This may indicate that slab inflections may also have influenced the apparent overshoot in the northern asperity. The overshoot may have caused a transfer of stresses from the interface to the upper plate that triggered the extensional deformation across the Pichilemu Fault. The correlation between interface geometry and slip is also observed for the case of the 1960 Valdivia earthquake to the south (Fig. 8), where slip concentration and termination coincide with slab inflections. So, the plate geometry may influence strain accumulation and release in a subduction zone, a process expected to act over long time scale encompassing more than one seismic cycle.

7. Conclusions

We have presented new estimates of static coseismic surface displacements measured by a dense GPS network and used them in conjunction with published geodetic data to obtain an updated, higher-resolution slip model of the 2010 Maule earthquake. The use of a FE-model that introduced the main geometrical complexities of the Chile subduction zone allowed us to compare the spatial relation of slip patterns before and during the 2010 Maule earthquake with tectonic features.

The theoretical accumulated slip deficit since the last great earthquake in 1835 suggests that the Maule earthquake has most likely closed the Concepción–Constitución seismic gap. Areas that concentrated high coseismic slip released more slip than has accumulated since 1835, suggesting a local overshoot or slip deficits inherited from former periods of strain accumulation, retained over more than one earthquake, as proposed for the 1960 segment to the south (Cisternas et al., 2005). The locking patches over the decade preceding the Maule earthquake are roughly coincident with the rupture extent, indicating some degree of persistence of asperities in the seismic cycle.

We found that updip as well as along-strike rupture limits appear to be controlled by splay faults, which take up part of plate convergence coseismically by converting elastic interseismic strain accumulated in the upper plate into permanent upper plate shortening, thus limiting rupture propagation. The Maule earthquake rupture does not correlate with any first-order bathymetric feature of the oceanic plate. Major gradients in coseismic slip spatially correlate with bends in the dip of the megathrust. This asymmetry can cause differential stresses that may induce a higher accumulation/release of seismic moment and affect also dynamic propagation of the rupture. Thus, correlations between co- and inter-seismic slip with long-term tectonic features suggest a tectonic control on slip patterns in the south-central Chile